



Assessment of creep-fatigue behavior, deformation mechanisms, and microstructural evolution of alloy 709 under accelerated conditions

T.D. Porter^{a,*}, K.O. Findley^a, M.J. Kaufman^a, R.N. Wright^b

^a Colorado School of Mines, 1500 Illinois St., Golden, CO 80401, USA

^b Idaho National Laboratory, 1955 Fremont, P.O. Box 1625, Idaho Falls ID 83415, USA

ARTICLE INFO

Keywords:

Alloy 709

Creep-fatigue

Microstructure evolution

Time-dependent deformation

Dynamic strain aging

ABSTRACT

Alloy 709 is a leading candidate structural material for sodium-cooled fast spectrum reactors (FSR), where creep-fatigue is a potential failure mode. Low cycle fatigue (LCF) and creep-fatigue tests with 30 min tensile hold times have been conducted to failure at 550 and 650 °C, corresponding to potential service and accelerated test temperatures, respectively. Creep-fatigue life is reduced relative to LCF at both temperatures, though significantly more at 550 °C compared to 650 °C. Differences in slip behavior, dynamic recovery, precipitate evolution, and strain-aging effects result in less stress relaxation and sustained high tensile stresses in creep-fatigue at 550 °C; thus, there is more intergranular damage compared to 650 °C.

1. Introduction

The improved economics of next generation nuclear reactors depend, in part, on improved performance of advanced structural materials. Power plant structural components, for both fossil and nuclear fuels, are subject to complex stress cycles at elevated temperature, which necessitates the use of highly corrosion- and creep-resistant alloys. An increase in operating temperature and component lifetime demands advancements of high-temperature structural alloys. Alloy 709 is a 20Cr-25Ni-1.5Mo-Nb-N solid solution and precipitation strengthened austenitic stainless steel developed by Nippon Steel for fossil boiler applications, implemented under ASME Code Case 2581 [1]. Alloy 709 is a candidate alloy for structural components in sodium cooled fast spectrum reactors (FSR) due to its improved creep resistance over the current structural alloys Type 316 stainless steel and Grade 91 [2]. Currently, Alloy 709 is only ASME code qualified in tubular form for fossil boiler applications, whereas nuclear structural components will be made from plate product form. ASME Boiler and Pressure Vessel (BPV) Code requires analysis of creep-fatigue performance for thick section nuclear components due to the thermomechanical fatigue experienced during start-up and shut-down of the reactor [3]. Creep-fatigue analysis is not required under the BPV code for fossil boiler applications, so little creep-fatigue data has been generated for performance assessment for this alloy.

In addition to the difference in product form, the proposed service conditions differ significantly between fossil and nuclear applications.

The expected service temperature for structural components of next generation FSRs is 550 °C, whereas boiler tubes typically experience service temperatures greater than 650 °C. Additionally, fossil boiler tubes have shorter life cycles than those required for nuclear structural components. Therefore, most of the published creep and microstructural data for Alloy 709 is at higher temperatures than typical FSR operating temperatures.

Accelerated creep and creep-fatigue testing, by means of testing at higher temperatures and greater strains than expected during service, is typically necessary to generate a statistically significant amount of data in a reasonable time. The creep-rupture data from accelerated creep tests are extrapolated to expected service conditions using a Larson-Miller plot to predict component life for creep conditions and as part of the creep-fatigue life analysis. However, it has been shown that extrapolation of accelerated test results to lower temperatures and smaller strains produces non-conservative creep rupture and creep-fatigue life predictions for Type 316L(N) stainless steel [4,5]. The non-conservative predictions are attributed to a change in time-dependent (creep) deformation mechanisms from power-law creep (climb then glide creep) in accelerated conditions to diffusional creep (Nabarro-Herring and Coble creep) in near-service conditions. Additionally, dynamic strain aging (DSA) is active in several nitrogen-containing stainless steels in the intermediate temperature range relevant to service conditions [5–10]. DSA is known to affect the deformation and damage mechanisms of stainless steels in low cycle fatigue (LCF) by promoting planar slip and preventing dynamic recovery [6,7,11,12]. The enhanced slip

* Corresponding author.

E-mail address: typorter@mines.edu (T.D. Porter).

<https://doi.org/10.1016/j.ijfatigue.2019.02.037>

Received 11 December 2018; Received in revised form 12 February 2019; Accepted 23 February 2019

Available online 25 February 2019

0142-1123/ © 2019 Elsevier Ltd. All rights reserved.

planarity, which contributes to high rates of strain hardening and slip band impingement on grain boundaries, can be detrimental to creep-fatigue life [8,9,13].

An initial investigation of creep-fatigue in Alloy 709 by the present authors showed significantly different behavior and cyclic life reduction compared to LCF at 550 and 650 °C [14]. The objective of the current investigation is to assess the deformation and damage mechanisms and microstructural evolution during creep-fatigue testing of Alloy 709 at an accelerated testing condition (650 °C) and the relationship to the near-service condition (550 °C). Differences in deformation behavior between accelerated testing and service conditions can result in significantly different creep-fatigue cyclic stress response, damage formation, and cyclic life. Additionally, the stability of the microstructure (i.e. second phase formation and dissolution) in austenitic stainless steels is known to have a significant effect on elevated temperature mechanical behavior. Evolution of the microstructure of Alloy 709 is also investigated at 550 and 650 °C to determine the effects on creep-fatigue performance. A comprehensive understanding of creep-fatigue behavior and microstructural evolution at accelerated testing and near-service conditions will provide a basis to develop reliable extrapolation models for Alloy 709 in nuclear reactor design.

2. Experimental procedure

Strain-controlled LCF tests, without and with (creep-fatigue) 30 min tensile hold periods, have been performed according to ASTM E2714 [15], using servo-hydraulic testing frames at Idaho National Laboratory (INL) on specimens machined from two solution annealed heats of Alloy 709, labeled 011593 and 011594. Tests were conducted to failure at the expected service temperature of 550 °C and an accelerated test temperature of 650 °C. Additionally, creep-fatigue tests were interrupted at various cycle intervals corresponding to regions of cyclic hardening, a maximum in cyclic tensile stress, and cyclic softening. All test conditions are summarized in Table 1. Fatigue tests to failure were performed on both experimental heats of material and all of the interrupted tests were performed on heat 011594. All tests were conducted in air using a symmetrical triangular waveform profile with $R = -1$, a strain rate ($\dot{\epsilon}$) of 10^{-3} s^{-1} , and a total strain range ($\Delta\epsilon_T$) of 1 pct. Strain was measured using a two-pronged extensometer. During testing, temperature was maintained by resistance heaters and monitored by thermocouples welded outside the gage section. Cylindrical button-head specimens were machined from the as-received annealed plates with the stress axis parallel to the rolling direction and longitudinal final polishing in the gage section to eliminate fatigue crack initiation sites. The number of cycles to failure is defined by a 20 pct decrease in the ratio of peak tensile to peak compressive stress, which indicates macroscopic crack initiation [16].

Two microstructurally different heats of Alloy 709 were used in this study, with compositions shown in Table 2. Both heats were processed at Oak Ridge National Laboratory (ORNL) by hot forging and rolling, then solution annealing at 1100 °C, followed by water quenching. The grain size and uniformity of the as-received microstructures of the two heats were compared by light optical microscopy (LOM). Specimens for LOM were mechanically polished and then electrolytically etched in a solution of 60 pct nitric acid in water with a current density of approximately 10 mA/cm^2 to delineate the grain boundaries without

revealing the annealing twins to the same level of contrast according to a procedure outlined in literature [17]. Grain size was determined using the concentric circle intercept method on five random areas according to ASTM E112 [18].

The effective length of intergranular cracks was quantified for each condition with a linear intercept method using light optical micrographs of polished specimens. Ten micrographs were taken 1 mm from the surface and ten were taken 2 mm from the surface along the gage sections of each sample. A random grid of vertical lines was overlaid on images where the cracks were primarily horizontal (normal to the loading axis). The number of crack intersections, N , was tabulated and the effective crack length, L_{eff} , was determined by,

$$L_{\text{eff}} = \frac{NA}{l_{\text{grid}}} \quad (1)$$

where A is the micrograph area in mm^2 and l_{grid} is the total length of gridlines [19].

Electron channeling contrast imaging (ECCI) was used to characterize deformation in the resulting microstructures. This technique shows contrast variations as a result of misorientation within the lattice due to boundaries, slip bands, or defects (i.e. dislocations and stacking faults) [12,20,21]. ECCI was performed on bulk samples from the gage sections of failed specimens using a JEOL® field emission scanning electron microscope (FESEM) in COMPO mode (signal of two backscatter electron detectors summed) with a scintillator type backscatter electron detector. The bulk nature of this technique allows for a much larger area to be analyzed than in a transmission electron microscope (TEM). Due to the sensitivity of ECC specimens to subsurface deformation from mechanical polishing, specimens were diamond polished to $0.5 \mu\text{m}$, followed by electropolishing with a solution of 10 pct perchloric acid in methanol, and finally vibratory polishing with $0.02 \mu\text{m}$ colloidal silica for up to 8 h.

TEM was used to analyze dislocation structures and precipitation in failed specimens. A Philips® CM12 and a FEI® Talos F200X TEM were used in this analysis, with accelerating voltages of 120 and 200 keV, respectively. TEM specimens were prepared from transverse slices through the gage section away from the fracture surface. 3 mm discs were electropolished on a Fishcienne® twin-jet electropolisher using a solution of 10 pct perchloric acid in methanol at a temperature of approximately -40°C .

Dislocation densities of the deformed microstructures were estimated from X-ray diffraction (XRD) line broadening. XRD scans were conducted on the same specimens used for ECCI deformation characterization. A PANalytical® X'Pert diffractometer was used with $\text{Cu K}\alpha$ radiation, a step size of 0.008° , a time per step of 100 s, and a 2θ range from 40 to 100° . A modified Williamson-Hall method was used to determine dislocation density, according to the procedure described by Ungar et al. [22]. The first five peaks of FCC austenite (111, 200, 220, 113, and 222) were used in this analysis, and each sample was scanned a total of four times to increase the statistical significance, with sample rotations between each scan.

Vickers microhardness testing was performed on the as-received material and the gage sections of each test specimen conducted to failure on heat 011594 according to ASTM E384 [23]. A grid of 50 indents and a 500 gf load was used on each sample.

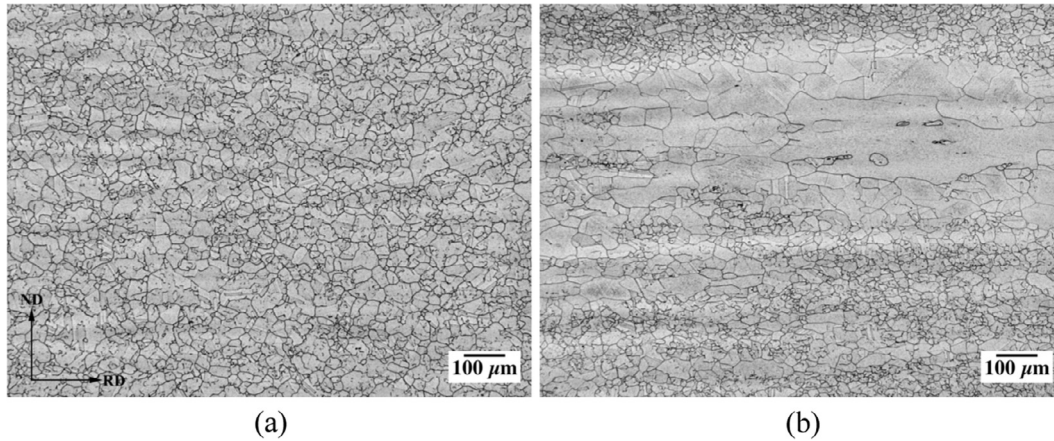
Table 1
LCF and creep-fatigue test matrix.

Temperature (°C)	Tensile hold time (min)	Total strain range, $\Delta\epsilon_T$ (pct)	Test end condition
550	0	1.0	To failure
550	30	1.0	To failure, Interrupted at 50, 400, and 600 cycles
650	0	1.0	To failure
650	30	1.0	To failure, Interrupted at 25, 50, and 400 cycles

Table 2

Compositions of experimental heats of alloy 709 (wt pct).

Heat ID	C	Mn	Si	Ni	Cr	Mo	Ti	Nb	N	S	P	B
011593	0.073	0.90	0.39	24.98	19.84	1.51	< 0.01	0.25	0.13	0.0008	< 0.005	0.004
011594	0.078	0.90	0.39	25.01	19.89	1.51	< 0.01	0.25	0.14	0.0006	< 0.005	0.0037

**Fig. 1.** Light optical micrographs of the as-received microstructures from heats (a) 011594 and (b) 011593 [14].

3. Results

3.1. Initial microstructural characterization

Light optical micrographs of the as-received (solution annealed) microstructures of the two heats of Alloy 709 used for this study are shown in Fig. 1 [14]. Heat 011594, shown in Fig. 1(a), has a uniform equiaxed grain structure with an average grain size of approximately 30 μm and an average hardness of 176 HV. Heat 011593, shown in Fig. 1(b), has a banded microstructure of non-uniform grain size and shape. This microstructure has bands of relatively large grains elongated in the rolling direction between larger regions with finer grain size and a narrower size distribution. In the uniform regions, the average grain size is approximately 20 μm , while in the bands of large grains the grain size is up to approximately 600 μm . The average hardness of 011593 is 193 HV. Both microstructures contain a significant amount of annealing twins.

The solution annealed microstructures contain a bi-modal size distribution of Nb(C,N) precipitates observed both intragranularly and intergranularly. Fine spherical precipitates with a diameter of approximately 100 nm are distributed relatively uniformly throughout the microstructure, while irregularly shaped precipitates ranging in size from approximately 500 nm to 10 μm are present in stringers aligned along the rolling direction. The fine precipitates formed during hot working and subsequent cooling, whereas the coarse precipitates likely formed during casting solidification. Both heats used in this study had similar initial precipitation volume fractions and distributions.

3.2. LCF and creep-fatigue

Peak tensile and compressive stress versus cycle number are shown in Fig. 2 for LCF and creep-fatigue tests at 550 and 650 $^{\circ}\text{C}$. During LCF at 550 $^{\circ}\text{C}$, the material cyclically hardens for the entire test, with a higher rate of hardening for approximately the first 200 cycles followed by a slower rate of hardening until the stress drops off as a result of crack formation and propagation. At 650 $^{\circ}\text{C}$, initial cyclic hardening occurs at a higher rate compared to 550 $^{\circ}\text{C}$ up to a maximum stress after approximately 100 cycles, followed by cyclic softening until failure. With the addition of a 30 min tensile hold (i.e. creep-fatigue), cyclic hardening at 550 $^{\circ}\text{C}$ is extended to approximately 400 cycles to a

maximum stress approximately 14 pct greater than in LCF. In creep-fatigue, unlike LCF, cyclic softening occurs after approximately 400 cycles at 550 $^{\circ}\text{C}$. In creep-fatigue at 650 $^{\circ}\text{C}$, the cyclic hardening regime is shortened to approximately the first 50 cycles to a maximum stress approximately 5 pct lower than in LCF. Subsequent cyclic softening at 650 $^{\circ}\text{C}$ occurs at a high rate initially, followed by a slower rate until failure.

For both LCF and creep-fatigue tests, the cyclic stress behavior (i.e. hardening and softening) was consistent between the two microstructures, though there was a slight variation in cycles to failure. These results suggest that the homogeneity of the grain structure does not have a significant impact on LCF or creep-fatigue performance under the specific conditions used in this study (i.e. smooth polished specimens machined with the stress axis parallel to the plate rolling direction).

The number of cycles to failure, N_f , for each test is presented in Table 2. In LCF, the tests at 550 $^{\circ}\text{C}$ had cyclic lives approximately twice those at 650 $^{\circ}\text{C}$. In creep-fatigue, however, the cyclic lives were approximately the same at both temperatures. Compared to LCF, the cyclic lives were reduced significantly at both temperatures with the introduction of a 30 min tensile dwell period, which is typical for austenitic stainless steels. The fatigue life reduction factor (FLRF), defined as N_f in creep-fatigue normalized by N_f in LCF, is a convenient metric to evaluate creep-fatigue lives compared to LCF for a given temperature, strain rate, and strain range [5]. At 650 $^{\circ}\text{C}$, the average FLRF is 0.51, i.e. a life reduction of approximately two when the hold time is imposed. The average FLRF at 550 $^{\circ}\text{C}$ is 0.24, i.e. a creep-fatigue life reduction of approximately four. The significant difference in the creep-fatigue life reduction between the two temperatures indicates that the 30 min tensile hold time is more damaging at 550 $^{\circ}\text{C}$ than 650 $^{\circ}\text{C}$ for Alloy 709.

Creep-fatigue hysteresis loops in the hardening regime for both temperatures are shown in Fig. 3. Serrated yielding is observed in the hysteresis loops at both temperatures, indicating solute pinning effects of DSA on mobile dislocations. The serration shape and frequency are significantly different between the two temperatures, with more frequent load drops at 550 $^{\circ}\text{C}$ and greater magnitude load drops at 650 $^{\circ}\text{C}$. Additionally, the serrations at 650 $^{\circ}\text{C}$ begin at larger strains with increasing number of cycles until they are almost completely non-existent in the tensile region after approximately 50 cycles. The disappearance of serrations at approximately 50 cycles coincides with the maximum

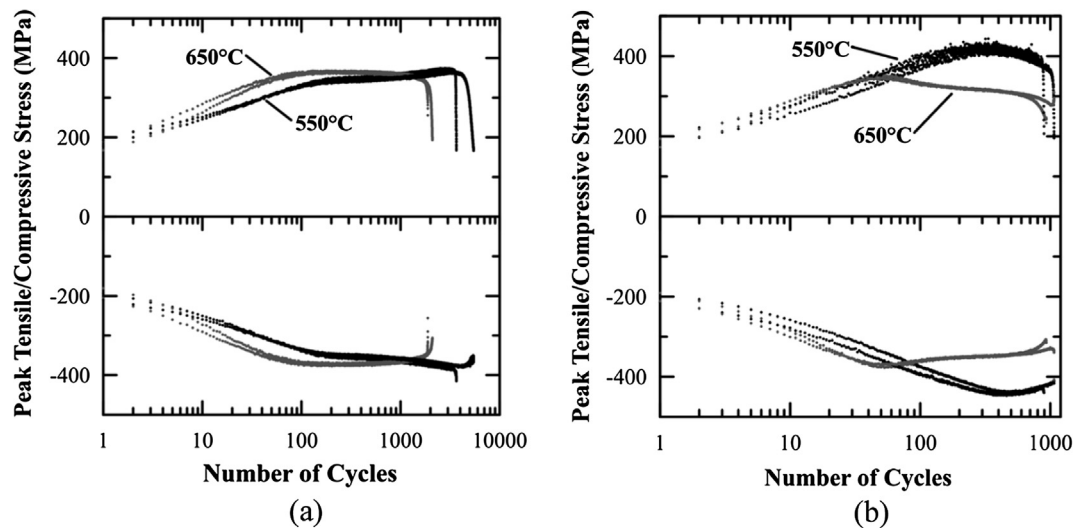


Fig. 2. Peak tensile and compressive stress at each fatigue cycle for (a) LCF and (b) creep-fatigue tests conducted to failure at 550 and 650 °C with $\Delta\epsilon_T = 1$ pct. Each of the four tests were performed on both heats of material.

peak tensile stress and the onset of cyclic softening. At 550 °C, serrations are observed up to approximately 400 cycles, which also coincides with a maximum in peak tensile stress. One loop in the softening region, cycle 250, is shown for 650 °C to demonstrate the disappearance of serrated yielding during cyclic softening.

Stress relaxation during the tensile hold in a creep-fatigue cycle, which is a decrease in stress due to the conversion of elastic strain into inelastic (i.e. creep) strain, is related to the time-dependent deformation mechanisms and the accumulated damage for each cycle. Fig. 4 shows stress as a function of time during the 30 min tensile hold of the approximate mid-life cycle ($N = 500$) at 550 and 650 °C. Despite the significantly higher stress at the beginning of the hold at 550 °C compared to 650 °C, the amount of stress relaxation is significantly less for the duration of the hold. Specifically, the stress relaxation at mid-life at 550 and 650 °C is approximately 20 and 110 MPa, respectively. The magnitude of stress relaxation is directly related to the amount of inelastic deformation that contributes to the width of the hysteresis loop (see Fig. 3). Thus, the amount of inelastic strain during the hold period (and the accumulation of inelastic strain throughout the duration of the test) is significantly greater at 650 °C than at 550 °C.

However, the magnitude of inelastic strain cannot always be related

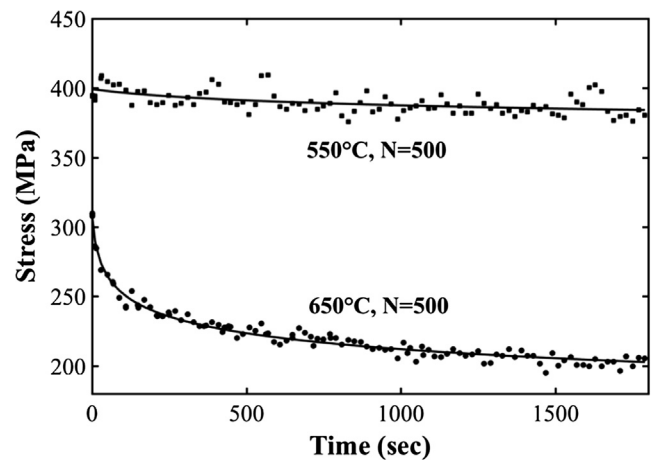


Fig. 4. Stress relaxation during the 30 min tensile dwell of cycle 500 (near mid-life) at 550 and 650 °C.

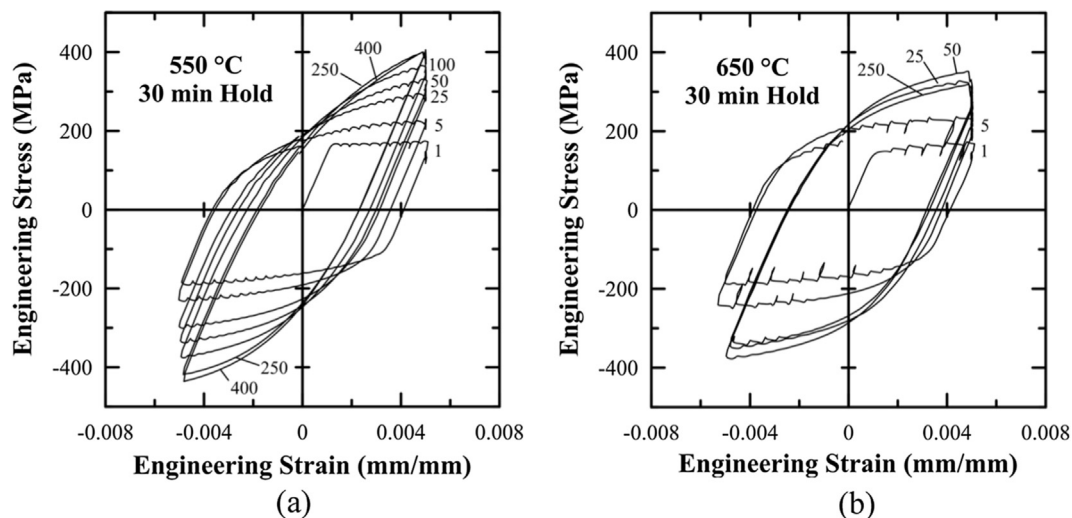


Fig. 3. Select cyclic hardening hysteresis loops from creep-fatigue tests on heat 011594 with $\Delta\epsilon_T = 1$ pct at (a) 550 °C and (b) 650 °C. The curves show differences in plastic strain range (loop width) and disappearance of serrated flow.

to the amount of intergranular damage or number of cycles to failure because the strain rate varies during relaxation and different strain rates correspond to different deformation mechanisms [7,24]. Depending on the alloy and the testing conditions, initial strain rates during relaxation may be high ($> 10^{-4} \text{ s}^{-1}$) and correspond to matrix plasticity rather than diffusion-controlled creep deformation, which occurs at lower strain rates. Analysis of strain rates during stress relaxation provides an understanding of the deformation mechanisms and their contribution to grain boundary damage accumulation. The inelastic strain rate, $\dot{\epsilon}_p$, can be related to the rate at which stress decreases, $\dot{\sigma}$, by Hooke's law:

$$\dot{\epsilon}_p = \frac{\dot{\sigma}}{E} \quad (2)$$

where E is the Young's modulus at the test temperature. The stress during the hold time is fit by linear regression to a power law relation, which can then be differentiated with respect to time to determine strain rate during the hold. For Alloy 709, the strain rates during stress relaxation at 550 °C are low and vary from 2.5×10^{-7} to $2.0 \times 10^{-8} \text{ s}^{-1}$. The relaxation strain rates at 650 °C are higher, ranging from 1.5×10^{-5} to $6.0 \times 10^{-8} \text{ s}^{-1}$. Since the relaxation strain rates at both 550 and 650 °C are below those expected for matrix deformation, it is interpreted that all of the inelastic strain accumulated during the hold is due to creep mechanisms. Thus, the larger range and greater magnitude of relaxation strain rates at 650 °C corresponds to a greater magnitude of creep deformation during the 30 min hold compared to 550 °C.

3.3. Characterization of tested microstructures

Microstructural characterization was performed on the gage sections of specimens from heat 011594 tested at both temperatures in LCF and creep-fatigue. The objective of the microstructural characterization was to correlate microstructural damage, dislocation structures, and precipitation to creep-fatigue behavior and life. The link between microstructure and creep-fatigue performance provides insight into the deformation and damage mechanisms active under accelerated and near-service test conditions.

3.3.1. Macroscopic and microscopic damage

Damage was qualitatively characterized for the LCF and creep-fatigue specimens by analysis of secondary crack density and crack mode. For both LCF and creep-fatigue conditions, the specimens tested at 550 °C have significantly fewer surface cracks away from the main fracture (i.e. secondary cracks) in the gage section than the specimens tested at 650 °C. Fig. 5 shows etched light optical micrographs of secondary cracks in all conditions tested to failure. For both temperatures, the LCF tests result in primarily transgranular cracks that originate at the specimen surface. In creep-fatigue, the fracture mode is primarily intergranular at 550 °C and mixed with transgranular and intergranular fracture at 650 °C.

Internal grain boundary cracks (i.e. away from surface crack tips) are present at end of life for both temperatures tested in creep-fatigue, but not in LCF. Intergranular cracks extend along grain boundaries normal to the loading direction. The morphology of intergranular cracks differs between the two temperatures in acuity and length. Intergranular cracks at 550 °C are sharper compared to the more blunted cracks at 650 °C. Additionally, more short and rounded cracks are present at 650 °C compared to 550 °C, which has cracks that frequently span across several grains.

Intergranular damage at end of life was quantified by the total effective intergranular crack length per area at 1 and 2 mm from the surface; the results are shown for both temperatures in Table 4. For both depths from the surface, the 550 °C condition has approximately twice the effective crack length compared to 650 °C. As shown in Table 3, the creep-fatigue lives are comparable at the two temperatures.

Thus, the internal damage accumulated during approximately the same number of cycles in creep-fatigue is significantly greater at 550 °C than at 650 °C, which correlates with a greater reduction in creep-fatigue life compared to LCF life at 550 °C.

3.3.2. Cyclically deformed dislocation structures

Dislocation structures were studied in the gage section of specimens tested to failure by both LCF and creep-fatigue tests at both temperatures. Fig. 6 shows representative ECCI micrographs from each of the conditions tested to failure, revealing significant differences in the deformation structures at each temperature in both LCF and creep-fatigue.

Following the LCF test at 550 °C, the dislocation structures are primarily planar, as shown by the linear slip band traces in the bottom left grain in Fig. 6(a). Loosely defined dislocation walls are observed in some grains, adjacent to grain or twin boundaries, as shown in the top grain of Fig. 6(a). Dislocation walls are defined here as dense clusters of dislocations between regions of the matrix without significant misorientation. Subgrain boundaries, on the other hand, are well-defined tilt or twist boundaries separating regions of the matrix with distinct misorientation, formed during recovery of dislocation walls. The matrix on either side of the dislocation walls at 550 °C shows little contrast variation, indicating that the walls are not recovered subgrain boundaries.

The resulting microstructure after LCF at 650 °C, as shown in Fig. 6(b), has significantly more well-defined dislocation walls and less frequent planar structures compared to LCF at 550 °C. Stark contrast variation across cell boundaries at 650 °C indicates recovered subgrain boundaries, which are not observed at 550 °C. Subgrains on the order of approximately 500 nm are frequently observed adjacent to grain and twin boundaries, as indicated by the arrows in Fig. 6(b). The formation of subgrains at 650 °C suggests dislocation rearrangement and annihilation to form well-defined boundaries, which is indicative of extensive dislocation cross-slip and climb.

Representative creep-fatigue deformation structures for 550 and 650 °C are shown in Fig. 6(c) and (d), respectively. In creep-fatigue at 550 °C, deformation within the grains consists primarily of planar slip bands, as with LCF. Well-defined dislocation walls are less frequent than in the LCF microstructure. However, subgrains with well-defined boundaries are sometimes present directly adjacent to grain boundaries, indicating more dynamic recovery in creep-fatigue than in the case of LCF. The resulting creep-fatigue microstructure at 650 °C is almost completely void of planar structures and dislocation walls. Instead, well-defined subgrains are adjacent to the majority of grain and twin boundaries and extend deeper into the grains than in LCF, as shown in Fig. 6(d). Extensive subgrain formation adjacent to boundaries in the 650 °C creep-fatigue microstructure is indicative of dynamic recovery and reduction of strain energy at the boundaries. It should be noted here that the white spherical precipitates shown in all ECCI micrographs are Nb(C,N) that are present in the solution annealed condition.

Fig. 7 shows representative low magnification bright field (BF) TEM micrographs of creep-fatigue microstructures for comparison to the ECCI micrographs. At 550 °C, deformation is restricted to primarily planar slip with dense slip bands impinging on grain and twin boundaries, as shown in Fig. 7(a). The dislocation density between the slip bands is relatively low, indicating heterogeneous deformation which results in stress concentrations at grain boundaries. Fig. 7(b) shows well-defined subgrains adjacent to a grain boundary (left) after creep-fatigue at 650 °C. Subgrains are observed in TEM in a similar size, morphology, and location as those seen in the ECCI micrographs.

3.3.3. Precipitation

Precipitation is significantly different in Alloy 709 after LCF and creep-fatigue testing at 550 and 650 °C. In LCF tests, the specimens were exposed to 550 °C for an average of 25 h (approximately 4000 cycles) compared to 12 h at 650 °C (approximately 2000 cycles). In

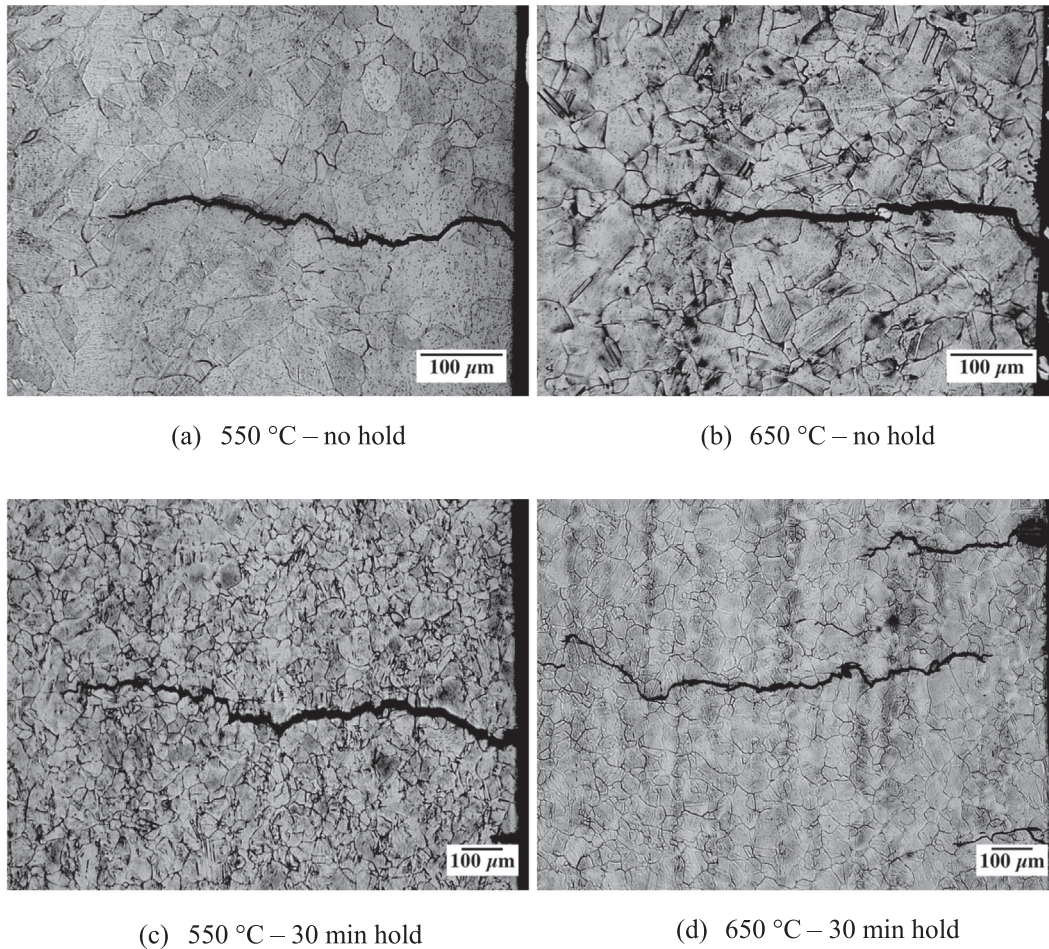


Fig. 5. Light optical micrographs of surface cracks from the gage sections of specimens from heat 011594 tested to failure in LCF at (a) 550 °C and (b) 650 °C and in creep-fatigue with a 30 min tensile hold at (c) 550 °C and (d) 650 °C. Transgranular cracking is typical for both temperatures tested in LCF. In creep-fatigue, fractures are primarily intergranular at 550 °C and mixed transgranular and intergranular at 650 °C. The specimen surface is on the right in all images.

Table 3
Cycles to failure for LCF and creep-fatigue tests.

Test temperature (°C)	Hold time (min)	Cycles to failure, N_f (011593, 011594)	Average FLRF
550	0	4964, 3629	0.24
550	30	888, 1062	
650	0	1883, 2047	0.51
650	30	1069, 931	

creep-fatigue tests, the specimens were exposed to each temperature for approximately the same time of 500 h (the number of cycles to failure was approximately 1000 for both temperatures). Following all test conditions, grain boundaries contain $M_{23}C_6$ precipitates. However, after creep-fatigue testing at 650 °C, grain boundary precipitates are significantly coarser and discrete compared to the rest of the conditions where precipitates are fine and continuous along the boundaries. The finer continuous grain boundary precipitation during creep-fatigue at 550 °C provides more nucleation sites for grain boundary voids, which likely contributes to the higher density of cracked boundaries compared to 650 °C.

LCF at 650 °C results in fine intragranular carbides clustered on dislocation cell walls and subgrain boundaries, which indicates that the dislocation structures provide heterogeneous nucleation sites for precipitation. Fig. 8 shows a TEM BF micrograph of approximately 20 nm cuboidal carbides clustered on dislocation walls in the 650 °C LCF condition; the precipitates were determined by selected area diffraction

(SAD) to be $M_{23}C_6$. After LCF at 550 °C, intragranular $M_{23}C_6$ carbides are observed less frequently than at 650 °C and are significantly smaller (less than 10 nm).

Creep-fatigue testing results in significant differences in intragranular precipitation between the two test temperatures. At 550 °C, $M_{23}C_6$ carbides are approximately 10–20 nm and decorate dislocations uniformly throughout the grains. Fig. 9(a) shows a BF TEM image of cuboidal carbides near a $[1\ 1\ 2]$ zone axis with a SAD inset showing the extra reflections from $M_{23}C_6$; the reflections confirm a cube-cube orientation relationship with the lattice and a lattice parameter approximately three times larger than the matrix. It should be noted here that the tilt conditions from the zone axis resulted in a disappearance of the dislocations in Fig. 9(a) to better show the precipitates. After creep-fatigue testing at 650 °C, the $M_{23}C_6$ carbides are significantly coarser (approximately 50 nm) and more uniformly distributed compared to the LCF condition. Fig. 9(b) shows the coarse $M_{23}C_6$ particles, along with very fine precipitates revealed by the Moiré fringes on dislocations (indicated by arrows on the figure). The inset SAD pattern of a $[1\ 1\ 2]$ zone shows extra reflections (circled), in addition to those from $M_{23}C_6$, which identify the fine precipitates as MX with a cube-cube orientation relationship to the matrix.

3.3.4. Dislocation density and hardness

Dislocation densities of the deformed microstructures have been estimated from XRD line broadening. Peak broadening in an XRD line profile is due to three factors: instrument broadening, crystallite size, and micro-strain from defects like dislocations. Deconvolution of the

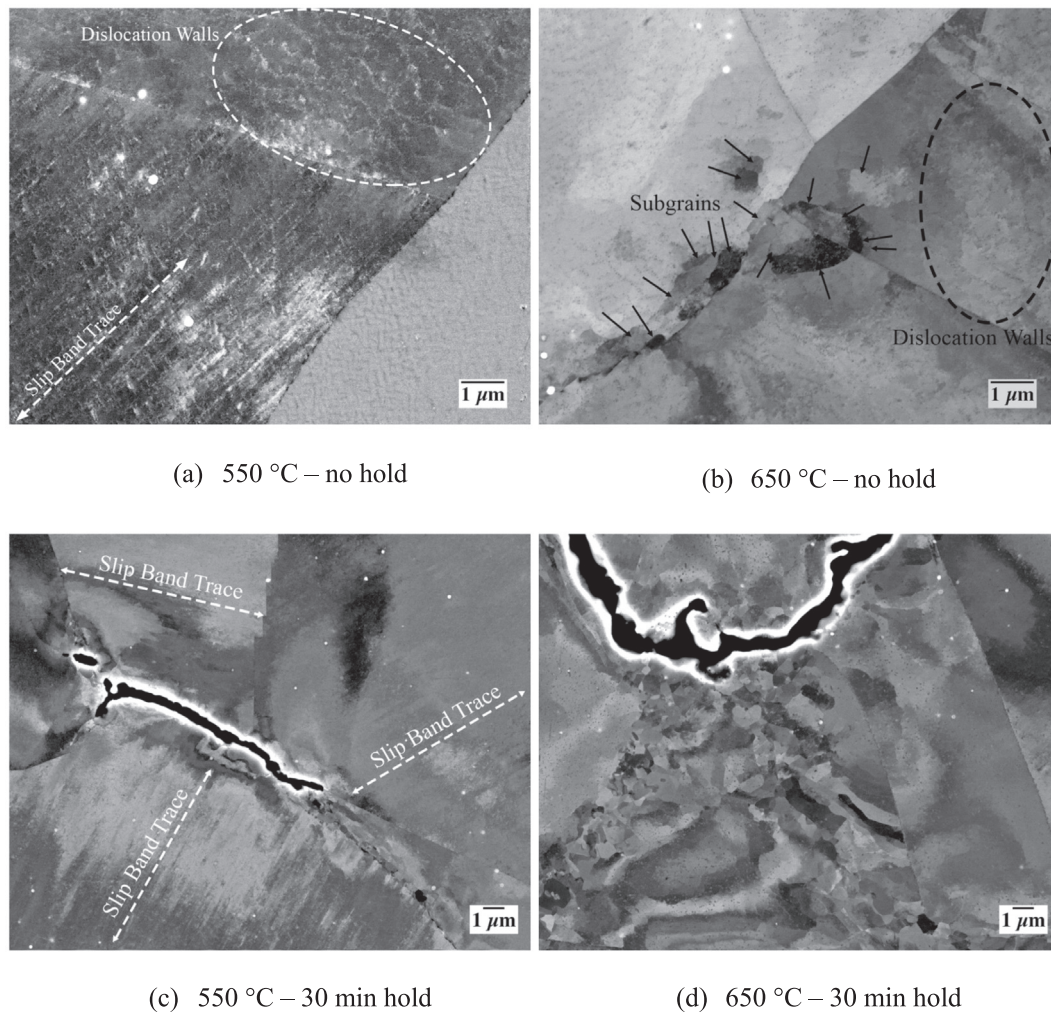


Fig. 6. ECCI micrographs of deformed microstructures from the gage sections of specimens from heat 011594 tested to failure in LCF at (a) 550 °C and (b) 650 °C and in creep-fatigue with a 30 min tensile hold at (c) 550 °C and (d) 650 °C. Slip band traces are indicated by arrows with broken lines in both 550 °C microstructures. Regions with dislocation walls are circled in both LCF microstructures. Subgrains are indicated by arrows in the 650 °C LCF condition. A higher density of subgrains is apparent below the crack in the 650 °C creep-fatigue microstructure.

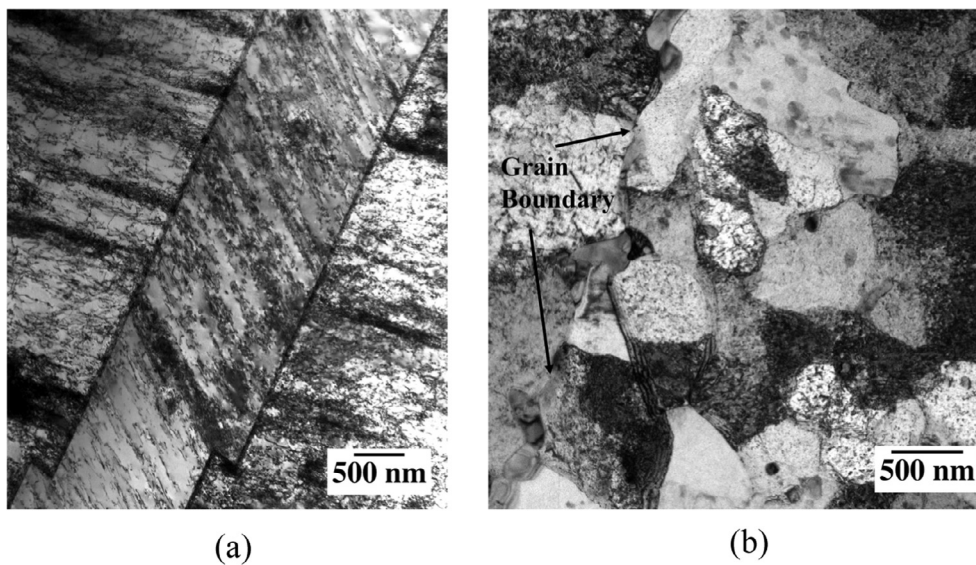


Fig. 7. TEM BF micrographs of resulting creep-fatigue dislocation structures in heat 011594 at (a) 550 °C and (b) 650 °C. Deformation at 550 °C is primarily planar with slip bands impinging on grain and twin boundaries (twin boundaries are shown in the figure). At 650 °C, well-defined subgrains are observed near boundaries (grain boundary on the left).

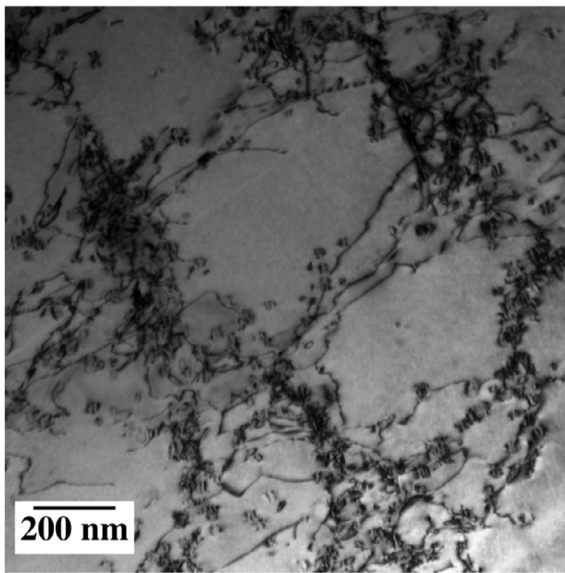


Fig. 8. TEM BF image of fine $M_{23}C_6$ precipitates after continuous cycling at 650 °C. The fine carbides are densely clustered on dislocation walls and in between the walls in a significantly lower density. This micrograph is taken from the gage section of a specimen from heat 011594.

broadening into these components can be done using an approach first proposed by Williamson and Hall [26] and modified by Ungar et al. [22] to account for dislocation strain anisotropy. Since broadening from small crystal (i.e. diffracting domain) size is not a function of the diffraction angle and strain broadening is, a plot of broadening versus angle produces a positive slope that is directly related to the amount of micro-strain or dislocation density in the sample.

Fig. 10(a) shows the estimated dislocation density for the four conditions tested to failure, alongside Vickers microhardness measurements of the same microstructures in Fig. 10(b). The dislocation density and room temperature hardness values show a similar trend; both values are greater after testing at 550 °C compared to 650 °C for both LCF and creep-fatigue. The higher dislocation density after LCF at 550 °C compared to 650 °C is consistent with the differences in the

cyclic stress response between the two test temperatures, i.e. cyclic hardening at 550 °C and cyclic softening at 650 °C. These results also agree with the qualitative TEM and ECCI observations of dislocation density and dislocation structures in the two LCF conditions. The dislocation density after creep-fatigue at 550 °C is approximately the same as the LCF test at the same temperature, within the range of measurement error. Similar dislocation densities after LCF and creep-fatigue tests suggests that no significant recovery occurs during the hold time at 550 °C, which is consistent with the small degree of stress relaxation in creep-fatigue. The slight increase in hardness in the creep-fatigue microstructure over LCF is likely due to the fine intragranular (~ 10 – 20 nm) $M_{23}C_6$ precipitates shown in Fig. 9(a).

Interestingly, the measured dislocation density after creep-fatigue at 650 °C is greater than that after LCF, despite having a lower peak stress prior to failure than the LCF test. Additionally, more recovery is evident in the deformed microstructures after creep-fatigue testing at 650 °C, which indicates a lower dislocation density in the creep-fatigue condition. The reason for the greater measured dislocation density in this condition may be due to additional peak broadening from coherency strains at the interface between the matrix and very fine MX precipitates, which are shown in Fig. 9(b). Coherency strains can contribute to the peak broadening because there are local regions where the lattice parameter deviates from the bulk of the matrix, thus leading to a range of possible Bragg diffracting conditions [27,28]. However, the hardness in the specimen tested in creep-fatigue at 650 °C is not significantly different than the LCF specimen tested at the same temperature, which indicates strength loss from dislocation recovery is compensated by strengthening from fine intragranular precipitates.

Dislocation density estimates and hardness measurements from the interrupted and failed microstructures are shown in Fig. 11. Dislocation density at 650 °C follows approximately the same trend as the peak stress versus cycle shown in Fig. 2; peak dislocation density occurs after 50 cycles, followed by a significant decrease after cyclic softening occurs. This result supports dynamic recovery being partly responsible for the observed cyclic softening during creep-fatigue testing at 650 °C. At 550 °C, dislocation density is approximately the same as 650 °C after 50 cycles and remains relatively unchanged until failure. This result indicates that the softening observed at 550 °C is due in larger part to grain boundary damage rather than microstructural recovery.

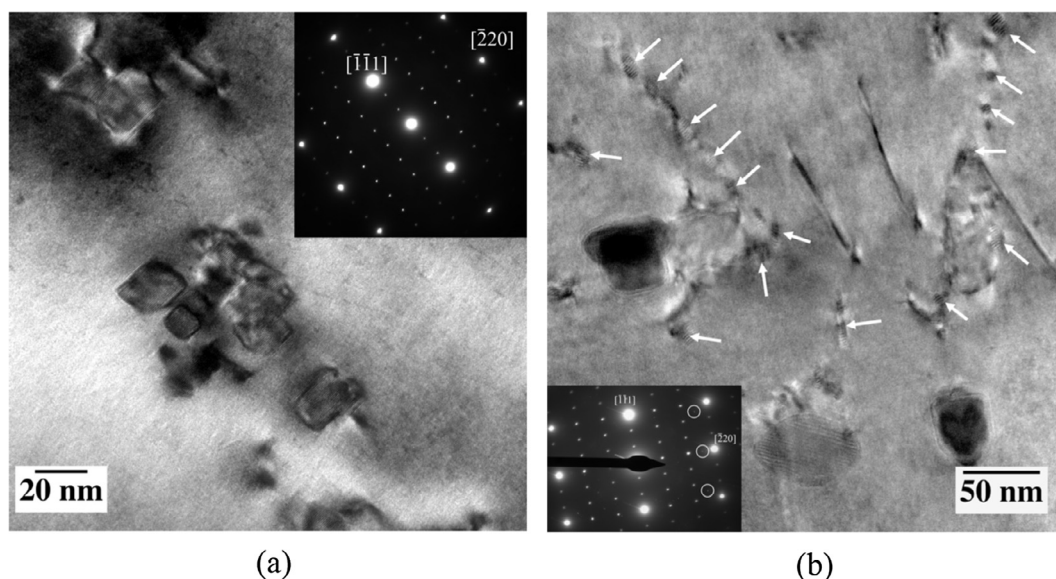


Fig. 9. TEM BF images of the resulting microstructure after creep-fatigue testing at (a) 550 °C showing cuboidal $M_{23}C_6$ precipitates and (b) 650 °C showing coarse $M_{23}C_6$ precipitates and a distribution of finer precipitates (arrows). Both micrographs are taken near a $[1\ 1\ 2]$ zone and have SAD insets down zone that show the $M_{23}C_6$ extra reflections as in (a) and additional reflections (circled in inset SAD) in (b) revealing the fine precipitates to be MX. Both micrographs were taken from gage sections of specimens from heat 011594.

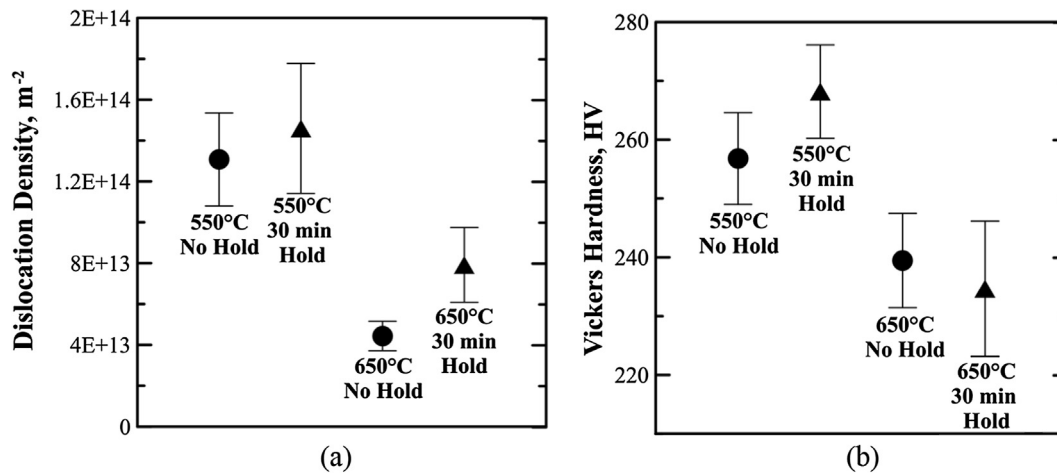


Fig. 10. (a) Estimated dislocation density and (b) Vickers hardness measurements and standard deviations from the gage sections of LCF and creep-fatigue test specimens from heat 011594. The resulting dislocation density and hardness were greater in both test conditions at 550 °C compared to 650 °C.

Room temperature hardness results for the interrupted tests are shown in Fig. 11(b). At 550 °C, hardness increases significantly after 50 cycles, which is a result of dynamic precipitation of fine carbides intragranularly. At 650 °C, a small decrease in hardness was observed after reaching a maximum at 50 cycles. Hardness does not decrease substantially despite a decrease in dislocation density; carbide formation during creep-fatigue offsets the hardness decrease due to the decrease in dislocation density. These results, combined with the microstructural characterization, support more significant dynamic recovery during creep-fatigue testing at 650 °C compared to 550 °C. A summary of the cyclic behavior and corresponding microstructural observations and measurements is provided in Table 5.

4. Discussion

4.1. Microstructural evolution and mechanical behavior

The LCF cyclic stress response (i.e. hardening or softening) of austenitic stainless steels depends on many factors including initial microstructure, solute-dislocation interaction, strain amplitude, strain rate, temperature, and hold time. Cyclic hardening is due to increasing dislocation interactions with obstacles such as other dislocations, grain

Table 4

Total effective intergranular crack length for failed creep-fatigue test samples (mm/mm^2).

Test Temperature (°C)	1–2 mm from surface	2–3 mm from surface
550	2.9 ± 0.8	2.6 ± 0.7
650	1.5 ± 0.4	1.4 ± 0.3

boundaries, and precipitates, and is common for well-annealed materials. Cyclic softening is attributed to recovery by dislocation annihilation and the formation of low energy dislocation structures (LEDs) such as persistent slip-bands (PSBs), walls/veins, cells, or low angle subgrains [25,29,30,31]. At sub-creep temperatures (i.e. below $\sim 0.4T_m$) the formation of LEDs requires extensive cross-slip of screw dislocations, while at higher temperatures, dislocation climb contributes significantly to dynamic recovery and cyclic softening. Slip behavior in materials where deformation is accommodated by extensive cross-slip is characterized as wavy, and is typical for materials with high stacking fault energy (SFE) where partial dislocations can more readily constrict to unit screw dislocations to cross-slip. Austenitic stainless steels, such as Type 316 and 304, are typically considered to deform by planar slip rather than wavy slip, which is attributed to their

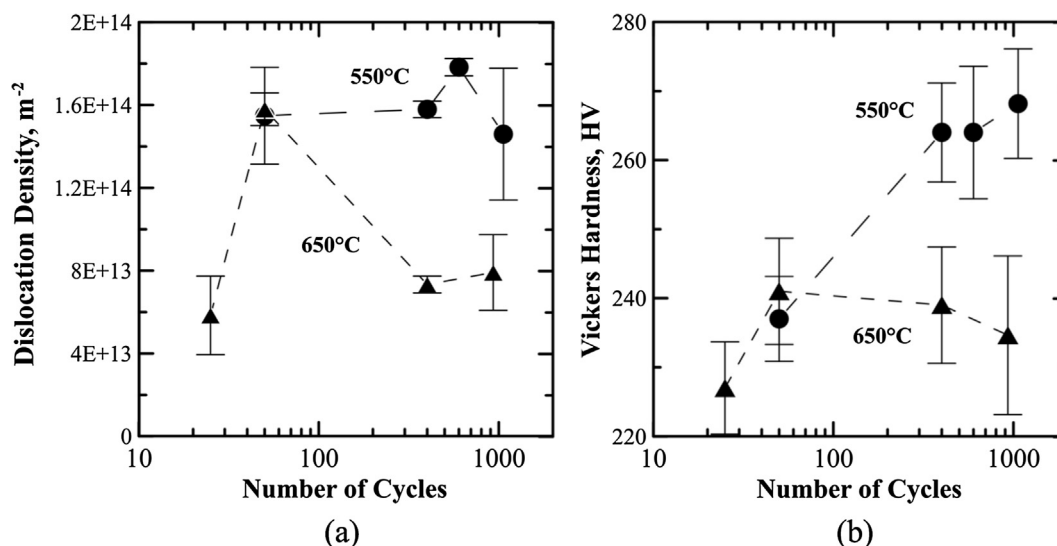


Fig. 11. (a) Estimated dislocation density and (b) Vickers hardness measurements and standard deviations from the gage sections of interrupted creep-fatigue test specimens from heat 011594.

Table 5
Summary of microstructural characterization and cyclic behavior for Alloy 709.

Temperature (°C)	Tensile hold time (min)	Cyclic behavior	Microstructural and fracture observations and measurements
550	0	Initial hardening (~200 cycles) followed by a slower rate of hardening	Primarily planar deformation; continuous fine grain boundary $M_{23}C_6$; little intragranular precipitation; transgranular fracture
650	0	Initial hardening (~100 cycles) followed by a slower rate of softening	Planar deformation with cell and subgrain formation near boundaries; grain boundary $M_{23}C_6$; fine (~30 nm) intragranular $M_{23}C_6$; transgranular fracture
550	30	Initial hardening (~400 cycles) to a maximum stress 14 pct greater than in LCF followed by softening; little stress relaxation; serrated flow to ~400 cycles	Primarily planar deformation; infrequent cellular/subgrain structures; constant dislocation density and increasing hardness after 50 cycles; fine continuous grain boundary $M_{23}C_6$; fine (~20 nm) intragranular $M_{23}C_6$; intergranular fracture
650	30	Initial hardening (~50 cycles) to a maximum stress 5 pct lower than in LCF followed by a slower rate of softening; significant stress relaxation; serrated flow to ~50 cycles	Significant subgrain formation; decreasing dislocation density and hardness after 50 cycles; coarse discrete grain boundary $M_{23}C_6$; fine (~50 nm) intragranular $M_{23}C_6$ and very fine (~8–10 nm) MX; mixed transgranular and intergranular fracture

low SFE [7,31]. However, high stresses in the vicinity of grain boundaries, where compatibility must be maintained, can induce cross-slip and the formation of LEDS in otherwise planar slip materials [25]. Several investigations have shown that cyclic deformation of such alloys results in the formation of LEDS, such as subgrains, which is associated with the onset of cyclic softening [12,30]. Therefore, a transition from cyclic hardening to softening indicates a transition in slip behavior from planar to wavy and the onset of recovery by cross-slip and/or climb.

The cyclic stress behavior of Alloy 709 in LCF and creep-fatigue is significantly different at 550 and 650 °C, for a given strain range and strain rate, which results from different deformation behavior at the two temperatures. Cyclic softening after initial cyclic hardening in LCF at 650 °C indicates the onset of dynamic recovery by cross-slip and/or climb, and the formation of LEDS. During LCF at 550 °C, only cyclic hardening occurs, due to primarily planar deformation and a lack of recovery for the duration of the test. Microstructural characterization supports primarily planar deformation at 550 °C and the transition to wavy slip character by cell and subgrain formation at 650 °C. Subgrains in the 650 °C LCF condition are observed adjacent to grain boundaries, where the highest compatibility stresses are expected. Dislocation density measurements further support dynamic recovery at 650 °C, where the resulting dislocation density is less than the LCF condition at 550 °C. Thus, the LCF cyclic stress behavior indicates a transition to wavy slip behavior after initial cyclic hardening at 650 °C, but not at 550 °C.

There are further differences in deformation behavior between creep-fatigue tests at 550 and 650 °C, i.e. with the addition of the 30 min tensile dwell. The creep-fatigue cyclic behavior at 650 °C is similar to the LCF behavior, except that the transition in deformation character from planar to wavy slip occurs after a smaller number of cycles, as shown by the earlier onset of cyclic softening compared to LCF. A significant decrease in dislocation density after the maximum peak stress at 50 cycles shows that the observed cyclic softening correlates with recovery. After creep-fatigue failure, the subgrain density is higher, boundaries are more well-defined, and subgrains extend further into the grains than in the LCF condition. Since the density of subgrains in the creep-fatigue microstructure is significantly greater than that observed in the LCF microstructure, it is interpreted that the increase in dynamic recovery is a result of the creep-strain during stress relaxation. Therefore, the relaxation strain rates at 650 °C, which are in the range expected for creep deformation rather than matrix plasticity, correspond to dislocation-mediated creep deformation (i.e. climb and glide) rather than diffusion-mediated deformation (i.e. Nabarro-Herring or Coble creep).

In creep-fatigue at 550 °C, a transition from cyclic hardening to softening occurs after approximately 400 cycles, which was not observed in LCF. However, this transition in the cyclic stress behavior is

not accompanied by significant subgrain formation or a decrease in dislocation density or hardness, as confirmed by the measurements from interrupted tests. The lack of significant microstructural recovery at failure indicates that the cyclic softening at 550 °C is primarily due to grain boundary cracking rather than dislocation-mediated strain energy minimization (i.e. cross-slip and/or climb). Additionally, creep deformation during the tensile hold is significantly smaller compared to 650 °C, as indicated by the narrow hysteresis loops and the magnitude of stress relaxation. Thus, regardless of the creep mechanism at 550 °C, the small amount of creep deformation is partly responsible for the lack of microstructural recovery and the sustained high tensile stresses at peak tensile strain.

Elevated temperature deformation (planar or wavy) in austenitic stainless steels is affected by the presence of solute atoms [32]. The presence of nitrogen is well-known to enhance the planar nature of cyclic deformation at intermediate temperatures and strain rates in austenitic stainless steels, which is attributed to DSA effects that prevent dislocation cross-slip necessary for the formation of LEDS [6]. Additionally, microstructural instabilities (i.e. precipitate formation and dissolution) during elevated temperature testing from an initially solution annealed condition may be responsible for changes in strengthening and deformation mechanisms in austenitic stainless steels. For example, high rates of initial cyclic hardening have been attributed to rapid intragranular precipitation during LCF and creep-fatigue in a high temperature ultra-fine precipitate strengthened (HT-UPS) alloy in which DSA does not occur and cannot account for the hardening [30]. In creep-fatigue of HT-UPS, a transition from cyclic hardening to softening occurs, which does not happen in LCF, and is attributed to precipitate bypass by dislocation climb during the hold time. For systems that exhibit both DSA and dynamic precipitation during testing, a delay and eventual disappearance of serrated flow occurs and is accompanied by a change in deformation character. The disappearance of serrated flow is attributed to dynamic precipitation, which depletes the solute concentration in the vicinity of mobile dislocations [33–35].

Serrated flow in the creep-fatigue hysteresis loops is present at both 550 and 650 °C for Alloy 709, which indicates active DSA under these conditions. Serrations in the hysteresis loops disappear after approximately 50 cycles at 650 °C and after approximately 400 cycles at 550 °C. The disappearance of serrated flow correlates with the onset of cyclic softening and the transition in slip behavior from planar to wavy at 650 °C. Additionally, the initial rate of cyclic hardening is greater at 650 °C than 550 °C in both LCF and creep-fatigue, which is attributed to a difference in precipitate strengthening early in the test between the two temperatures. After both LCF and creep-fatigue, the volume fraction and size of carbides at 650 °C are significantly greater than at 550 °C, indicating faster nucleation and growth at 650 °C. In creep-fatigue, the intragranular carbides after testing at 550 °C (approximately

500 h) are present in a similar size and morphology to those in the 650 °C LCF condition (after approximately 12 h). The $M_{23}C_6$ carbides in the 650 °C creep-fatigue microstructure are significantly coarser (~50 nm) than the LCF condition and a uniform dispersion of fine (~10 nm) MX carbides are also present. A significantly greater consumption of solute atoms in the formation and growth of carbides at 650 °C is likely responsible for the disappearance of serrated flow after approximately 50 creep-fatigue cycles. The reduced DSA corresponds with enhanced tendency for cross-slip and the formation of LEDS. Significant $M_{23}C_6$ coarsening during cycling at 650 °C may also contribute to the onset of cyclic softening simply due to a loss of strength and easier dislocation bypass. Slower precipitate nucleation at 550 °C is responsible for a slower rate of initial cyclic hardening in LCF and creep-fatigue. The slower growth of the precipitates at 550 °C results in cyclic hardening for a longer duration than at 650 °C since the solute concentration remains high enough to maintain strain-aging effects and the precipitates remain small enough to effectively pin dislocations. Thus, the significantly higher tensile stresses achieved in creep-fatigue at 550 °C are attributed to prolonged DSA effects, finer precipitation, and less creep deformation compared to 650 °C. The higher tensile stresses resulting from these factors are responsible for a greater amount of intergranular damage and creep-fatigue life reduction at 550 °C compared to 650 °C.

4.2. Microstructural evolution and damage formation during creep-fatigue

In most austenitic stainless steels and nickel alloys, the creep-fatigue life (with a tensile dwell) is reduced compared to pure LCF, and is typically accompanied by a shift in failure mode from primarily transgranular to primarily intergranular fracture [7,30,36]. Intergranular damage is generally characterized by grain boundary cavitation or wedge cracking from grain boundary sliding due to creep deformation processes (i.e. vacancy diffusion). Several mechanisms for creep cavity nucleation have been suggested including impingement of slip-bands on grain boundaries leading to high stress concentrations, nucleation on second phase particles at grain boundaries, and nucleation at grain boundary triple points as a result of grain boundary sliding [7]. The mechanism for void nucleation from slip-band impingement may be due to diffusional flow of vacancies to a region of high tensile stress (i.e. Nabarro-Herring or Coble creep). Alternatively, the stress concentration at the grain boundary may be high enough to form a crack nucleus without significant grain boundary or matrix diffusional flow. Grain boundary precipitates are generally considered beneficial to resist creep deformation by grain boundary sliding, and thus prevent wedge cracking. However, stress concentrations at the matrix/particle interface can lead to void nucleation by decohesion or diffusional processes. Cyclic loading leads to the growth and linkage of grain boundary cavitation damage, which results in fewer numbers of cycles to failure than in the absence of significant creep damage.

At both temperatures tested in this investigation, a significant decrease in the number of cycles to failure in creep-fatigue compared to LCF is accompanied by a change in fracture mode from primarily transgranular to primarily intergranular at 550 °C and mixed transgranular/intergranular at 650 °C. This result is consistent with a higher contribution of creep damage (i.e. grain boundary damage) with the introduction of a tensile hold time. The amount of inelastic creep deformation during the hold period is significantly greater at 650 °C than at 550 °C, which would indicate a greater amount of creep cavitation damage at 650 °C. However, the amount of grain boundary damage is significantly greater at 550 °C, despite the small amount of creep deformation. Therefore, it is hypothesized that differences in microstructural evolution (i.e. deformation structures, dislocation-solute interactions, and precipitation) during creep-fatigue testing at the two temperatures results in different mechanisms for damage formation and propagation.

The creep-fatigue life reduction in austenitic stainless steels

containing nitrogen is significantly greater compared to the same alloys with low nitrogen content [8,9]. The shorter creep-fatigue lives are attributed to enhanced slip planarity and a lack of dynamic recovery in nitrogen-containing alloys, leading to high cyclic stresses and large stress concentrations at grain boundaries from slip-band impingement. In Alloy 709, DSA is initially active at both 550 and 650 °C in creep-fatigue, indicating that the slip is primarily planar. The disappearance of serrated flow after the initial cyclic hardening at 650 °C, which is attributed to a reduction of the strain-aging effect, is accompanied by the onset of cyclic softening and dynamic recovery by dislocation cross-slip and climb. Consumption of solute atoms responsible for DSA is due to inter- and intragranular carbide precipitation at 650 °C. The formation of subgrains adjacent to grain boundaries at 650 °C significantly reduces stress concentrations from impinging slip bands, and therefore, reduces the driving force for damage formation and propagation. Additionally, the grain boundary precipitates coarsen relatively quickly at 650 °C, which reduces the interfacial surface area and number of void nucleation sites.

At 550 °C, little recovery is observed in the creep-fatigue microstructure and serrated flow and cyclic hardening continue up to approximately 400 cycles, resulting in significantly higher peak tensile stresses compared to 650 °C. Although the magnitude of stress relaxation is small, which results in high stresses at grain boundaries for the entire hold, the associated strain rates are indicative of creep deformation. Additionally, fine continuous grain boundary precipitates provide a high density of potent void nucleation sites. Thus, creep cavitation damage is expected during the tensile holds at 550 °C, though the amount is likely less compared to 650 °C. However, a higher density of grain boundary cracks at failure at 550 °C indicates that the damage is not purely due to creep cavitation. Thus, it is hypothesized that at 550 °C the high grain boundary stresses from impinging planar slip bands and a lack of recovery are responsible for the propagation of grain boundary cavities (formed at fine grain boundary precipitates), resulting in intergranular cracks extending over several grain diameters. The differences in the morphology of grain boundary cracks at the two temperatures provides support for different mechanisms of damage formation and propagation. Grain boundaries cracks at 650 °C are shorter with blunt crack tips compared to intergranular cracks at 550 °C, which are significantly longer with sharper crack tips. Long sharp cracks at 550 °C indicate less plasticity during crack propagation, e.g. through void nucleation and coalescence.

5. Conclusions

1. During the tensile hold at 550 °C, sustained high stresses result in a significantly higher degree of grain boundary damage and a greater reduction of creep-fatigue life (relative to the LCF life) compared to creep-fatigue and LCF tests performed at 650 °C. This result indicates that extrapolation of creep-fatigue behavior and life from accelerated testing at elevated temperatures in this study is not indicative of lower temperature behavior. This finding has implications in using accelerated testing to predict service behavior in sodium-cooled nuclear reactors.
2. During creep-fatigue testing, a greater magnitude in stress relaxation was observed during the tensile hold at 650 °C and corresponds to a higher degree of time-dependent creep deformation compared to 550 °C.
3. The disappearance of serrated yielding in the hysteresis loops corresponds to the onset of cyclic softening, a decrease in dislocation density, and a change in dislocation slip behavior from primarily planar to wavy at 650 °C. This change in slip behavior at 650 °C leads to the formation of LEDS (subgrains) through cross-slip and climb, as the strain aging effect on slip planarity is reduced.
4. Deformation structures and dislocation density measurements indicate that dynamic recovery mechanisms, such as subgrain formation and dislocation annihilation, are more active at 650 °C than

at 550 °C. Subgrain formation adjacent to grain boundaries at 650 °C reduces stress concentrations compared to impinging planar slip bands present at 550 °C. Thus, there is a lower degree of grain boundary damage at end of life at 650 °C compared to 550 °C, where no significant recovery is observed.

5. Significant differences in microstructural evolution (i.e. dynamic precipitate nucleation and growth) and the corresponding evolution in strengthening mechanisms have profound effects on the cyclic hardening rate, maximum tensile stress, and the onset of cyclic softening during LCF and creep-fatigue at 550 and 650 °C. A faster rate of precipitate nucleation and coarsening at 650 °C from an initially annealed condition is responsible for a higher initial rate of cyclic hardening, a reduction of the solute strain aging effect, and the onset of cyclic softening at a smaller number of cycles than at 550 °C.
6. Grain boundary precipitation is finer and more continuous after creep-fatigue testing at 550 °C compared to 650 °C. Since grain boundary precipitates are potent void nucleation sites during creep, a higher density of sites is available at 550 °C, which is partly responsible for the increased grain boundary damage.
7. Variations in the homogeneity of the grain structure in the two conditions evaluated in this study does not have a significant impact on LCF and creep-fatigue behavior or cyclic life under the testing conditions used in this study.

Acknowledgements

The authors gratefully acknowledge the efforts of Joel Simpson and Michael McMurtrey at Idaho National Laboratory for the LCF and creep-fatigue testing and Olivia DeNonno at Colorado School of Mines for the hardness testing. Additionally, the authors express gratitude for the support of this research, which was conducted through funding by the U.S. Department of Energy (DOE) Nuclear Energy University Program (NEUP) award 15-8548.

References

- [1] Cases of the ASME Boiler and Pressure Vessel Code, Code Case 2581, Section I, ASME International; 2007.
- [2] Y. Yamamoto, P.J. Maziasz, T.L. Sham, Report on the optimization and testing results of advanced austenitic alloys, Internal Report, Oak Ridge National Laboratory, ORNL/TM-2012/401; 2012.
- [3] "Rules for Construction of Nuclear Facility Components," Boiler and Pressure Vessel Code – 2015 edition, Section III, ASME International, 2015.
- [4] Rieth M, Falkenstein A, Graf P, Heger S, Jäntschi U, Klimiankou M, Materna-Morris E, Zimmermann H. Creep of the austenitic steel AISI 316 L(N). *Sci Rep* 2004.
- [5] Sauzay M, Mottot M, Allais L, Noblecourt M, Monnet I, Perinet J. Creep-fatigue behavior of an AISI Stainless Steel at 550 °C. *Nucl Eng Des* 2004;232:219–36.
- [6] Mannan SL. Role of dynamic strain ageing in low cycle fatigue. *Bull Mater Sci* 1993;16(6):561–82.
- [7] Rodriguez P, Bhanku Sankara Rao K. Nucleation and growth of cracks and cavities under creep-fatigue interaction. *Prog Mater Sci* 1993;37(1):403–78.
- [8] Reddy GVP, Sandhya R, Sankaran S, Parameswaran P, Laha K. Creep – fatigue interaction behavior of 316LN austenitic stainless steel with varying nitrogen content. *Mater Des* 2015;88:972–82.
- [9] Nilsson, J. O., "Effect of Nitrogen on Creep-Fatigue Interaction in Austenitic Stainless Steels at 600 °C," Low Cycle Fatigue, ASTM STP 942, H. D. Solomon, G. R. Halford, L. R. Kaisand, and B. N. Leis, Eds., American Society for Testing and Materials, Philadelphia, pp. 543–557, 1988.
- [10] Tsuzaki K, Hori T, Maki T, Tamura I. Dynamic strain aging during fatigue deformation in Type 304 austenitic stainless steel. *Mater Sci Eng* 1983;61:247–60.
- [11] Valsan M, Nagesha A. Low cycle fatigue and creep-fatigue interaction behaviour of 316L(N) stainless steel and its welds. *Trans Indian Inst Met* 2010;63(2–3):209–15.
- [12] Zauter R, Petry F, Christ H. J and Mughrabi H, "Thermomechanical Fatigue of the Austenitic Stainless Steel AISI 304L," Thermomechanical Fatigue Behavior of Materials, ASTM STP 1186, H. Sehitoglu, Ed., American Society for Testing and Materials, Philadelphia, pp. 70–90; 1993.
- [13] Srinivasan VS, Valsan M, Sandhya R, Sankara KB, Mannan SL, Sastry DH. High temperature time-dependent low cycle fatigue behaviour of a type 316L(N) stainless steel. *Int J Fatigue* 1999;21:11–21.
- [14] Porter T, Findley K, McMurtrey M. Assessment of creep-fatigue behavior of alloy 709. *Trans Am Nuclear Soc* 2017;117:559–62.
- [15] "Standard Test Method for Creep-Fatigue Testing", E2714-13, Annual Book of ASTM Standards, West Conshohocken, PA: ASTM International; 2013.
- [16] Totemeier T, Tian H. Creep-fatigue – environment interactions in INCONEL 617. *Mater Sci Eng, A* 2007;470:81–7.
- [17] Bell FC, Sonon DE. Improved metallographic etching techniques for stainless steel and for stainless steel to carbon steel weldments. *Metallography* 1976;9:91–107.
- [18] "Standard Test Methods for Determining Grain Size," E112-13, Annual Book of ASTM Standards, West Conshohocken, PA: ASTM International; 2013.
- [19] Underwood E., "Quantitative Stereology for Microstructural Analysis," Microstructural Analysis, J. McCall and W. Mueller, Eds., Springer, Boston; 1973.
- [20] Ahmed J, Wilkinson A, Roberts S. Characterising dislocation structures in bulk fatigued copper single crystals using electron channelling contrast imaging (ECCI). *Phil Magazine* 1997;76:237–45.
- [21] Kaneko Y, Fukui K, Hashimoto S. Electron channeling contrast imaging of dislocation structures in fatigued austenitic stainless steels. *Mater Sci Eng, A* 2005;401:413–7.
- [22] Ungar T, Dragomir I, Revesz A, Borbely A. The contrast factors of dislocations in cubic crystals: the dislocation model of strain anisotropy in practice. *J Appl Crystallogr* 1999;32:992–1002.
- [23] "Standard Test Method for Microindentation Hardness of Materials", E384-16, Annual Book of ASTM Standards, West Conshohocken, PA: ASTM International; 2016.
- [24] Hales R. A method of creep damage summation based on accumulated strain for the assessment of creep-fatigue endurance. *Fatigue Eng Mater Struct* 1983;6:121–35.
- [25] Li Y, Laird C. Cyclic response and dislocation structures of AISI 316L stainless steel. Part 2: polycrystals fatigued at intermediate strain amplitude. *Mater Sci Eng, A* 1994;186:87–103.
- [26] Williamson GK, Hall WH. X-ray line broadening from filed aluminium and wolfram. *Acta Metallurgica* 1953;1:22–31.
- [27] Kuzel R, He B, Houska CR. Characterization of severe matrix distortions during phase separation from the redistribution of diffracted intensities. *J Mater Sci* 1997;32:2451–67.
- [28] Novelo-Peralta O, González G, Lara-Rodriguez GA. Characterization of precipitation in Al–Mg–Cu alloys by X-ray diffraction peak broadening analysis. *Mater Charact* 2008;59:773–80.
- [29] Laird C, Charsley P, Mughrabi H. Low energy dislocation structures produced by cyclic deformation. *Mater Sci Eng* 1986;81:433–50.
- [30] Carroll MC, Carroll LJ. Fatigue and creep-fatigue deformation of an ultra-fine precipitate strengthened advanced, austenitic alloy. *Mater Sci Eng, A* 2012;556:864–77.
- [31] Mughrabi H, Ackermann F, Herz K. Persistent Slipbands in Fatigued Face-Centered and Body-Centered Cubic Metals. West Conshohocken, PA: ASTM International; 1979. p. 69–105.
- [32] Hong SI, Laird C. Mechanisms of slip mode modification in F.C.C. solid solutions. *Acta Metallurgica et Materialia* 1990;38:1581–94.
- [33] Beese AM, Wang Z, Stoica AD, Ma D. Absence of dynamic strain aging in an additively manufactured nickel-base superalloy. *Nat Commun* 2018;9.
- [34] Hayes RW. On a proposed theory for the disappearance of serrated flow in F.C.C. Ni alloys. *Acta Metall* 1983;31(3):365–71.
- [35] Nalawade SA, Sundararaman M, Kishore R, Shah JG. The influence of aging on the serrated yielding phenomena in a nickel-base superalloy. *Scr Mater* 2008;59:991–4.
- [36] Wareing J. Creep-fatigue interaction in austenitic stainless steels. *Metall Mater Trans A* 1977;8A:711–21.